

© 2023 IEEE. Personal use of this material is permitted. Permission from IEEE must be obtained for all other uses, in any current or future media, including reprinting/republishing this material for advertising or promotional purposes, creating new collective works, for resale or redistribution to servers or lists, or reuse of any copyrighted component of this work in other works.

Simsek, Ergun, Ishraq Md Anjum, and Curtis R. Menyuk. "Solving Drift Diffusion Equations on Non-Uniform Spatial and Temporal Domains." In 2023 Photonics & Electromagnetics Research Symposium (PIERS), 1644–51, 2023. <https://doi.org/10.1109/PIERS59004.2023.10221464>.

<https://doi.org/10.1109/PIERS59004.2023.10221464>

Access to this work was provided by the University of Maryland, Baltimore County (UMBC) ScholarWorks@UMBC digital repository on the Maryland Shared Open Access (MD-SOAR) platform.

Please provide feedback

Please support the ScholarWorks@UMBC repository by emailing scholarworks-group@umbc.edu and telling us what having access to this work means to you and why it's important to you. Thank you.

Solving Drift Diffusion Equations on Non-uniform Spatial and Temporal Domains

Ergun Simsek, Ishraq Md Anjum, and Curtis R. Menyuk

Department of Computer Science and Electrical Engineering
University of Maryland Baltimore County, Baltimore, MD 21250, USA

Abstract— Drift-diffusion equations are solved with the finite difference method that involves nonuniform discretization of the spatial and temporal domains. By using a broadband window function as the modulation method, we achieve to calculate the quantum efficiency, phase noise, bandwidth, and response time of various types of photodetectors in a single run on a desktop computer.

1. INTRODUCTION

Photodetectors convert light into electrical signals and are commonly used in a wide range of applications that include metrology, optical communication systems, cameras, and LIDAR systems for autonomous vehicles. Drift-diffusion equations that can be solved with the finite difference method are often used to study the electrical behavior of these photodetectors. This approach is a useful compromise between Monte-Carlo simulations that are too complex to model the complex geometry of modern-day devices and purely empirical models that have limited predictive power. The drift-diffusion equations model the creation of electron-hole pairs in the presence of light and the movement of both electrons and holes in the semiconductor layers of the photodetector. The electrons and holes are effectively modeled as continuous fluids.

From quantum efficiency to phase noise, bandwidth to response time, various metrics can be used to describe the performance of a photodetector. A traditional yet moderately effective approach for obtaining these metrics is to solve the drift-diffusion equations assuming single frequencies for excitation and modulation with the finite-difference method as is done for example in [1, 2]. Using uniform grids in both the spatial and temporal domains simplifies both the formulation and implementation of these equations. However, this approach reduces the overall computational efficiency. Using a non-uniform spatial grid in which the maximum allowable mesh density in a given layer is chosen according to the refractive index of the material and increasing the mesh density near the boundaries between the neighboring layers makes it possible to reduce the number of unknowns while securing the desired accuracy level. Similarly, using large time steps when the fields and current are not significantly changing inside the domain of interest and using smaller time steps when they are expected to change can help with reducing the number of time steps used for the dynamic analysis. From the spectral point of view, studying non-linear devices such as photodetectors at unique excitation and modulation frequencies is a very safe choice but again not an efficient one from a computational point of view. Utilization of broadband modulation can be used to provide a broad RF response for such devices.

In this work, we address all of these issues by implementing a drift-diffusion equations solver with a finite-difference method that uses a non-uniform discretization of the spatial and temporal domains [3] and uses a broadband window functions as the modulation method [4, 5] to calculate the metrics of the photodetectors in a single run on a regular desktop computer. Comparison of the numerical results with experiments confirm the high accuracy of the proposed approach that yields a two-orders-of-magnitude reduction in computation time.

The outline of this paper is as follows: We first provide a brief summary of the drift-diffusion equations to analyze one-dimensional photodetectors consisting of an arbitrary number of semiconducting layers. Then, we briefly discuss the details of our one-dimensional computational model. In the third section, we present our numerical results for a photodetector that was studied experimentally in [6]. Finally, we provide some comments and conclusions.

2. FORMULATION AND IMPLEMENTATION

2.1. Drift-diffusion Equations

Our formulation starts with the electron and hole continuity equations and the Poisson equation,

$$\begin{aligned}\frac{\partial(p - N_A^-)}{\partial t} &= -\frac{1}{q}\nabla \cdot \mathbf{J}_p + G_{ii} + G_{opt} - R(n, p), \\ \frac{\partial(n - N_D^+)}{\partial t} &= +\frac{1}{q}\nabla \cdot \mathbf{J}_n + G_{ii} + G_{opt} - R(n, p), \\ \nabla \cdot \mathbf{E} &= \frac{q}{\epsilon}(n - p + N_A^- - N_D^+),\end{aligned}\tag{1}$$

where n is the electron density, p is the hole density, t is time, q is the unit of charge, \mathbf{J}_n is the electron current density, \mathbf{J}_p is the hole current density, R is the recombination rate, G_{ii} and G_{opt} are impact ionization and optical generation rates, \mathbf{E} is the electric field at any point in the device, ϵ is the electrical permittivity, N_A^- is the ionized acceptor concentration, and N_D^+ is the ionized donor concentration. The electron and hole current densities are governed by the equations

$$\mathbf{J}_p = qp\mathbf{v}_p(\mathbf{E}) - qD_p\nabla p \quad \text{and} \quad \mathbf{J}_n = qn\mathbf{v}_n(\mathbf{E}) + qD_n\nabla n,\tag{2}$$

where $\mathbf{v}_n(\mathbf{E})$ and $\mathbf{v}_p(\mathbf{E})$ are the electric-field-dependent electron and hole drift velocities, D_n and D_p are the electron and hole diffusion coefficients, respectively. We use the following empirical expressions for $\mathbf{v}_n(\mathbf{E})$ and $\mathbf{v}_p(\mathbf{E})$ to fit the measured results

$$\mathbf{v}_n(\mathbf{E}) = \frac{\mu_n(\mu_n + v_{n,sat}\beta|\mathbf{E}|)}{1 + \beta|\mathbf{E}|^2} \quad \text{and} \quad \mathbf{v}_p(\mathbf{E}) = \frac{\mu_p v_{p,sat} \mathbf{E}}{(v_{p,sat}^\gamma + \mu_p^\gamma |\mathbf{E}|^\gamma)^{1/\gamma}},\tag{3}$$

where μ_n is the electron low-field mobility, $v_{n,sat}$ is the saturated electron velocity, β is a fitting parameter, μ_p is the hole low-field mobility, γ is an empirical fitting parameter that depends on temperature, and $v_{p,sat}$ is the saturated hole velocity. To take into account the dependence of electron and hole low field mobilities, μ_n and μ_p , on the doping density, we define

$$\mu_{n,p} = \frac{\mu_{n_0,p_0}}{1 + \left(\frac{N_D + N_A}{N_{ref}}\right)^\eta},\tag{4}$$

where μ_{n_0} and μ_{p_0} are electron and hole mobilities at low doping concentrations, respectively, while N_{ref} and η are empirical parameters. The electric field dependent electron and hole diffusion coefficients are calculated with [7]

$$D_n(\mathbf{E}) = \frac{k_B T \mu_n / q}{\left[1 - 2(|\mathbf{E}|/E_p)^2 + \frac{4}{3}(|\mathbf{E}|/E_p)^3\right]^{1/4}} \quad \text{and} \quad D_p(\mathbf{E}) = \frac{k_B T}{q} \frac{\mathbf{v}_p(\mathbf{E})}{\mathbf{E}},\tag{5}$$

where E_p is the electric field at which the diffusion constant peaks. The main contribution to the recombination rate in Eq. (1) is the Shockley-Read-Hall (SRH) effect, which yields [8]

$$R = \frac{np - n_i^2}{\tau_p(n + n_i) + \tau_n(p + n_i)},\tag{6}$$

where τ_n , τ_p , and n_i are the electron and hole lifetimes and intrinsic carrier density respectively.

The optical generation rate in Eq. (1) is $G_{opt}(x, t) = G_c(t)e^{-\alpha(L-x)}$, where α is the absorption coefficient, x is distance across the device, L is the device length, and $G_c(t)$ is the generation rate coefficient as a function of time, which is given by $G_c(t) = \alpha P_{opt}(t)/AW_{photon}$, where $P_{opt}(t)$ is the optical power as a function of time, A is the area of the light spot, and W_{photon} is the photon energy [9]. Note that the generation rate in the absorption layer depends on the location in the device as well as the material. The total output current is the sum of the hole, electron, and displacement currents, i.e., $J_{total} = J_n + J_p + \epsilon \partial E / \partial t$.

Our model accounts for the incomplete ionization of doping impurities such as boron, aluminum, and nitrogen, using the following expressions [9, 10],

$$\begin{aligned} N_D^+ &= \frac{N_D}{1 + g_D \exp\left(\frac{E_C - E_D}{k_B T}\right) \exp\left(\frac{E_{Fn} - E_C}{k_B T}\right)}, \\ N_A^- &= \frac{N_A}{1 + g_A \exp\left(\frac{E_A - E_V}{k_B T}\right) \exp\left(-\frac{E_{Fp} - E_V}{k_B T}\right)}, \end{aligned} \quad (7)$$

where N_D and N_A are the donor and acceptor impurity concentrations, g_D and g_A are the respective ground-state degeneracy of donor and acceptor impurity levels [2, 11], E_A and E_D are the acceptor and donor energy levels, E_C and E_V are the low conduction band and the high valence band energy levels, E_{Fn} and E_{Fp} are the quasi-Fermi energy levels for the electrons and holes, and T is the temperature. The electron and hole generation rate due to impact ionization G_{ii} can be described as [12]

$$G_{ii} = \alpha_n \frac{|\mathbf{J}_n|}{q} + \alpha_p \frac{|\mathbf{J}_p|}{q}, \quad (8)$$

where α_n and α_p are the impact ionization coefficients of the electrons and holes, respectively. We calculate their values using the formulae [12, 13]

$$\alpha_n = A_n \cdot e^{-B_n/|\mathbf{E}|} \quad \text{and} \quad \alpha_p = A_p \cdot e^{-B_p/|\mathbf{E}|}, \quad (9)$$

where A_n , B_n , A_p , and B_p are experimentally-determined parameters [13, 14].

2.2. One-dimensional Computational Model

The implicit Euler method is used to discretize the drift-diffusion equations in time t for numerical computation. The spatial discretization along x is done non-uniformly, so that the spatial sampling density increases near the interfaces between neighboring layers.

For a photodetector that detects high-peak-power, ultra-short optical pulses, we need to have a sufficient number of points around the pulse to capture the rapidly changing fields and currents along the photodetector. In order to achieve this, we proposed a novel nonuniform time-stepping method in [3] as follows. We first divide the simulation time t into two parts t_A and t_B , where t_A is the time steps from $t = 0$ to $t = t_c$, where t_c is the pulse center, and t_B is the time steps from $t = t_c$ to $t = t_R$, where t_R is the pulse repetition period. t_B is determined by using the following expressions

$$t_B[\ell] = t_c + \left(\frac{t_R - t_c}{\sum_{k=1}^M \xi(k)} \right) \sum_{k=1}^{\ell} \xi(k), \quad (10)$$

$$\xi(k) = \{t_{\log,B}[k] - t_{\log,B}[k-1]\} \left(\frac{k + c_1}{M + c_1} \right)^{c_2}, \quad (11)$$

where $t_{\log,B}[\ell] = t_R^{(\ell-1)/(M-1)} t_c^{(M-\ell)/(M-1)}$ for $i = 1, 2, \dots, M$, c_1 and c_2 are coefficients that we can choose to control the amount we shrink/enlarge $\Delta t[\ell]$. A similar set of formulas is used to determine t_A and $t_{\log,A}$. Note that we define $t_{\log,B}[0] = t_{\log,B}[1]$, so that $t_B[1] = t_c$.

Figure 1 schematically shows the mesh that we use to discretize the x -dimension. We define the hole density p , the electron density n , and the electric potential φ , at the integer points in the mesh that are indexed by $l = 1, 2, \dots, N$. The current and electric field are defined at intermediate points that are indexed by $l = 3/2, 5/2, \dots, N - 1/2$. We define the distance between the integer points l and $l + 1$ as h_l , and the distance between the intermediate points $l - 1/2$ and $l + 1/2$ as h'_l . We set $h'_l = (h_{l-1} + h_l)/2$ and we approximate the electric field at the half-integer points in the mesh as $E_{l+1/2} = -(\psi_{l+1} - \psi_l)/h'_l$, where ψ_l is the potential at mesh-point l .

We approximate $\partial p/\partial x$ and $\partial n/\partial x$ at the half-integer points as

$$\left. \frac{\partial p}{\partial x} \right|_{l+1/2} = \left(\frac{p_{l+1} - p_l}{h'_l} \right) \quad \text{and} \quad \left. \frac{\partial n}{\partial x} \right|_{l+1/2} = \left(\frac{n_{l+1} - n_l}{h'_l} \right). \quad (12)$$

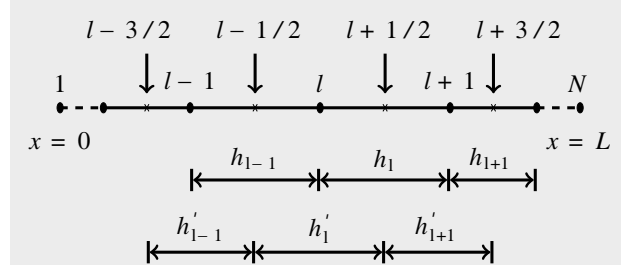


Figure 1: Numerical mesh used for the finite difference spatial discretization of the 1-D drift-diffusion equation.

We calculate the currents at the half-integer points by discretizing Eq. (2) to obtain

$$\begin{aligned} \mathbf{J}_{p,l+1/2} &= qp_{l+1/2} \mathbf{v}_{p,l+1/2}(\mathbf{E}) - qD_{p,l+1/2} \left(\frac{p_{l+1} - p_l}{h_l} \right), \\ \mathbf{J}_{n,l+1/2} &= qn_{l+1/2} \mathbf{v}_{n,l+1/2}(\mathbf{E}) + qD_{n,l+1/2} \left(\frac{n_{l+1} - n_l}{h_l} \right), \end{aligned} \quad (13)$$

where $p_{l+1/2} = (p_{l+1} + p_l)/2$, $n_{l+1/2} = (n_{l+1} + n_l)/2$, $D_{n,l+1/2}$ and $D_{p,l+1/2}$ are the electron and hole diffusion coefficients at the point $l + 1/2$, and $\mathbf{v}_{n,l+1/2}$ and $\mathbf{v}_{p,l+1/2}$ are the electron and hole drift velocities at the point $l + 1/2$.

Using this mesh, we discretize Eq. (1) so that it becomes

$$\begin{aligned} \frac{n_l^{i+1} - n_l^i}{\Delta t_\ell} &= \frac{1}{q} \frac{J_{n,l+1/2}^{i+1} - J_{n,l-1/2}^{i+1}}{h'_l} + G_l^{i+1} + G_{i,l}^{i+1} - R_l^{i+1}, \\ \frac{p_l^{i+1} - p_l^i}{\Delta t_\ell} &= -\frac{1}{q} \frac{(J_p)_{l+1/2}^{i+1} - (J_p)_{l-1/2}^{i+1}}{h'_l} + G_l^{i+1} + G_{i,l}^{i+1} - R_l^{i+1}, \\ \frac{1}{h'_l} \left[\frac{\varphi_{l+1}^{i+1} - \varphi_l^{i+1}}{h_l} - \frac{\varphi_l^{i+1} - \varphi_{l-1}^{i+1}}{h_{l-1}} \right] &= -\frac{q}{\epsilon} (N_{Dl}^+ - N_{Al}^- + p_l^{i+1} - n_l^{i+1}), \end{aligned} \quad (14)$$

where n_l^{i+1} and p_l^{i+1} are the electron and hole densities at the point l and time-step $i+1$, respectively, G_l^{i+1} is the generation rate at the point l and time-step $i+1$, R_l^{i+1} is the recombination rate at the point l and time-step $i+1$, φ_l^{i+1} is the electrostatic potential at the point l and time-step $i+1$, and finally N_{Dl}^+ and N_{Al}^- are the ionized donor and acceptor doping densities at the point l .

At the heterojunction interface x_0 that we show in Figure 2, the discretization is different due to a discontinuity in the hole density. Figure 2 shows a schematic illustration of the discretization in this case. We treat the drift-diffusion equation as a differential equation in the hole density, assuming that all other variables are constant across the grid, and we integrate across the grid element to obtain the hole density at the interface x_0 . The integration is done in two steps, first from x_l to x_0 and then from x_0 to x_{l+1} , as illustrated in Figure 2. The drift-diffusion equation for holes, which is obtained by inserting Eqs. (3) and 5 into Eq. (2), can be written as a differential equation in the hole density,

$$\frac{\partial p}{\partial x} = \frac{qE}{k_B T} p - \frac{E J_p}{k_B T v_p}. \quad (15)$$

Integrating from x_l to x_0 yields

$$p_{x_0^-} = p_l \exp \left[\frac{qE_{l+1/2}}{k_B T} \Delta x_1 \right] - \frac{J_{p,l+1/2}}{qv_{p,l+1/2}} \left\{ 1 - \exp \left[\frac{qE_{l+1/2}}{k_B T} \Delta x_1 \right] \right\}. \quad (16)$$

The integral from x_0 to x_{l+1} yields:

$$p_{x_0^+} = p_{l+1} \exp \left[-\frac{qE_{l+1/2}}{k_B T} \Delta x_2 \right] - \frac{J_{p,l+1/2}}{qv_{p,l+1/2}} \left\{ 1 - \exp \left[-\frac{qE_{l+1/2}}{k_B T} \Delta x_2 \right] \right\}. \quad (17)$$

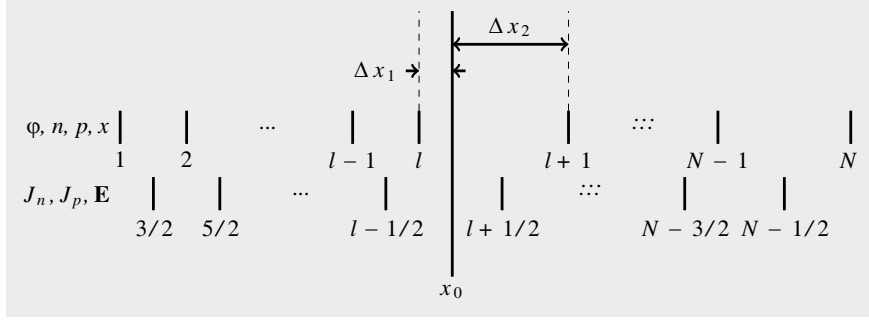


Figure 2: Discretization scheme that we used in our device model at a heterojunction interface.

2.3. Excitation Methods

We assume a monochromatic excitation to calculate the quantum efficiency and phase noise of a photodetector. If a continuous laser illumination is assumed, then we calculate these features in two steps. We first calculate the steady state output current. Then, we perturb the generation rate by ΔG_{opt} and calculate the impulse response due to the perturbation $\Delta G_{\text{opt}} = r G_{\text{opt}} \text{sech}[(t - t_c)/\tau]$, where r is the perturbation coefficient and τ is the impulse-width. The normalized impulse response $h(t)$ is equal to $\Delta I_{\text{out}}(t)/\int_0^\infty \Delta I_{\text{out}}(t)dt$, so that $\int_0^\infty h(t)dt = 1$, where $\Delta I_{\text{out}}(t)$ is the change in the output current due to the impulse. We calculate the phase noise in photodetectors as follows

$$\langle \Phi_n^2 \rangle = \frac{1}{N_{\text{tot}}} \frac{\int_0^{T_R} h(t) \sin^2 [2\pi n(t - t_c)/T_R] dt}{\left\{ \int_0^{T_R} h(t) \cos [2\pi n(t - t_c)/T_R] dt \right\}^2}. \quad (18)$$

A broadband modulation can be defined in various ways, for example with a sinc or a window function. In this work, three of the most commonly used windowing functions are implemented: the minimum four-term Blackman-Harris, the four-term continuous third derivative Nuttall, and the five-term flat-top by using the following expression

$$F_{\text{mod}}(t) = \frac{1}{L} \sum_{n=0}^N a_n \cos \left(\frac{2\pi n(t - t_c)}{L} \right) \text{ for } |t - t_c| \leq \frac{L}{2}, \quad (19)$$

where $f_{\text{mod}}^{\text{max}}$ is the highest frequency of interest and $L = 1/f_{\text{mod}}^{\text{max}}$. The coefficients $\{a_n\}_0^N$ are real constants that determine the characteristics of the windowing function. The rules for selecting the values of a_n may be found in [15, 16]. We use the values listed in Table 1.

Table 1: The coefficients in the broadband window function for the minimum 4-term Blackman-Harris window, continuous third derivative Nuttall window, and flat-top window. We note that different references provide slightly different coefficients, e.g., [15] and [16]. As long as we normalize the pulse in the time domain with its maximum value so that $\max[F_{\text{mod}}(t)] = 1$ and we normalize the power spectrum so that $P_{\text{out}}(f = 0)$, these differences do not significantly change the final results.

Type	a_0	a_1	a_2	a_3	a_4
Blackman-Harris	0.3532	0.488	0.145	0.01	—
Nuttall	0.3389	0.4819	0.161	0.018	—
Flat-Top	0.2155	0.4166	0.277	0.0836	0.0069

For the monochromatic modulation, the output power is simply $I_{\text{rms}}^2(t) \times R_{\text{load}}$, where R_{load} is the load resistance. For the broadband-window modulation, the different frequencies are not represented at the same strength, and we must normalize the spectrum of $I_{\text{rms}}^2(t) \times R_{\text{load}}$ with respect to the square of the absolute value of the FFT of $F_{\text{mod}}(t)$, so that

$$P_{\text{out}}(f_i) = \frac{|\text{FFT of } I_{\text{rms}}^2(t) \times R_{\text{load}} \text{ at } f_i|}{|\text{FFT of } F_{\text{mod}}(t) \text{ at } f_i|^2}. \quad (20)$$

3. NUMERICAL RESULTS

To verify the accuracy and efficiency of the formulation and its implementation, we choose the photodetector, that is studied experimentally in [6]. This photodetector belongs to the family of uni-traveling carrier (UTC) photodetectors. The doping and material types and doping concentrations are listed in Table 2. Different than typical UTCs, this design includes a thin p -doped layer in the middle of its depletion region. The diameter of the photodetector is $22\text{ }\mu\text{m}$. The load resistance is $50\text{ }\Omega$.

Table 2: Doping and material types, layer thicknesses, and doping concentrations for the each layer of a uni-traveling carrier photodetector experimentally studied in [6].

Doping & Mat. Type	Thickness (nm)	Doping Conc. (cm^{-3})
$p+$ InGaAs	50	2×10^{19}
$p+$ InP	300	2×10^{19}
p InGaAs	100	5×10^{18}
p InGaAs	100	2.5×10^{18}
p InGaAs	100	1×10^{18}
p InGaAs	100	5×10^{17}
InGaAsP, Q1.4	15	—
InGaAsP, Q1.1	15	—
$n-$ InP	10	2.5×10^{17}
$n-$ InP	280	1×10^{16}
$n-$ InP	20	5×10^{17}
$n-$ InP	300	1×10^{16}
$n+$ InP	200	1×10^{19}
$n+$ InGaAs	20	1×10^{19}
$n+$ InP	1000	1×10^{19}

Table 3 lists the parameters of InP and InGaAs that are used in our calculations. The material properties of InGaAsP layers can be found based on the listed Q -value [17].

Table 3: Material parameters at 300 K that are used in our calculations.

Parameter	InP	$\text{In}_{0.53}\text{Ga}_{0.47}\text{As}$
E_g (eV)	1.28	0.74
χ (eV)	4.38	4.51
ϵ_r (eV)	12.4	13.7
A_n (cm^{-1})	1.12×10^7	6.64×10^7
B_n (V/cm)	6.2×10^6	4×10^6
A_p (cm^{-1})	4.79×10^6	9.34×10^7
B_p (V/cm)	2.55×10^6	2.26×10^6
$\mu_{n,0}$ ($\text{cm}^2/\text{V sec}$)	5300	13000
$\mu_{p,0}$ ($\text{cm}^2/\text{V sec}$)	200	630
N_C (cm^{-3})	5.71×10^{17}	2×10^{17}
N_V (cm^{-3})	1.14×10^{19}	5.48×10^{18}
$N_{n,\text{ref}}$ (cm^{-3})	10^{17}	10^{17}
$N_{p,\text{ref}}$ (cm^{-3})	6×10^{17}	10^{18}
η_n	0.34	0.5
η_p	0.64	0.45
β (cm^2/V^2)	8×10^{-8}	4×10^{-8}
$v_{n,\text{sat}}$ (cm/sec)	6.7×10^6	7.67×10^8
$v_{p,\text{sat}}$ (cm/sec)	5×10^6	6.39×10^6
m_n^*/m_0	0.08	0.041
m_p^*/m_0	0.64	0.59

Figure 3(a) shows the electric field profiles along the photodetector under three different reverse-bias values ($V_{\text{bias}} = -7, -9, -11$ V) assuming a continuous wave laser illumination ($\lambda = 1550$ nm). Figure 3(b) shows how the electron, hole, displacement, and total currents change as a function of time for the $V_{\text{bias}} = -11$ V case. Note that the maximum value of the total current is close to the measured value (60 mA) that is reported in [6]. In Figure 3(c), we compare our numerical results for the normalized RF response with the measured ones. Again, we observe a good agreement. Lastly, we plot the phase noise as a function of the comb-line frequency in Figure 3(d), where we can see that the photodetector operates in a highly linear regime. There are — of course — some differences between the measured results and our numerical results. Considering the fact that there are more than 20 parameters used to describe semiconducting materials in our model, which depend on various factors such as temperature, doping density, local electric field intensity, etc., we consider our numerical results are close enough to the experimental results.

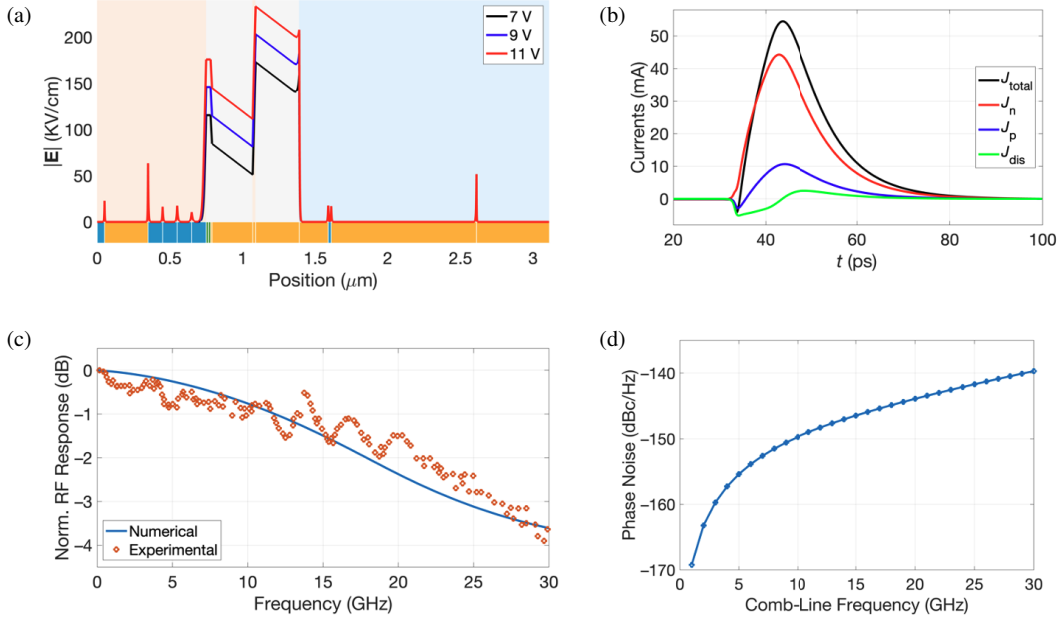


Figure 3: (a) Electric field profiles under different reverse bias voltages. (b) Current vs. time, where the red, blue, green, and black curves represent electron, hole, displacement, and total currents, respectively. (c) Calculated (blue curve) vs. measured (red circles) [6] normalized RF response as a function of frequency. (d) Phase noise as a function of comb-line frequency.

4. CONCLUSION

In conclusion, the drift-diffusion equations model is a useful approach for studying the electrical behavior of photodetectors due to its balance between complexity and predictive power. A finite difference method can be used to solve these equations, but a traditional approach of using single frequencies and uniform grids can limit computational efficiency. The implementation of a non-uniform spatial and temporal discretization, along with the use of broadband window functions as the modulation method, has proven to be a high-accuracy and efficient approach for calculating photodetector metrics. This approach results in a significant reduction in computation time and has been confirmed by comparison with experimental results.

ACKNOWLEDGMENT

The authors would like to acknowledge the funding from the US Naval Research Laboratory (Award No. N00173-21-1-G901).

REFERENCES

1. Mahabadi, S. E. J., S. Wang, T. F. Carruthers, C. R. Menyuk, F. J. Quinlan, M. N. Hutchinson, J. D. McKinney, and K. J. Williams, "Calculation of the impulse response and phase noise of

- a high-current photodetector using the drift-diffusion equations,” *Opt. Express*, Vol. 27, No. 3, 3717–3730, 2019.
2. Hu, Y., B. S. Marks, C. R. Menyuk, V. J. Urick, and K. J. Williams, “Modeling sources of nonlinearity in a simple p-i-n photodetector,” *J. Lightwave Technol.*, Vol. 32, 3710–3720, 2014.
 3. Simsek, E., I. Md Anjum, T. F. Carruthers, and C. R. Menyuk, “Non-uniform time-stepping for fast simulation of photodetectors under high-peak-power, ultra-short optical pulses,” *22nd International Conference on Numerical Simulation of Optoelectronic Devices*, Online, September 12–16, 2022.
 4. Simsek, E., I. Md Anjum, T. F. Carruthers, C. R. Menyuk, D. A. Tulchinsky, K. J. Williams, and J. C. Campbell, “Efficient and accurate calculation of photodetector RF output power,” *2022 IEEE Photonics Conference (IPC)*, Vancouver, Canada, November 13–17, 2022.
 5. Simsek, E., I. Md Anjum, T. F. Carruthers, C. R. Menyuk, J. C. Campbell, D. A. Tulchinsky, and K. J. Williams, “Fast evaluation of RF power spectrum of photodetectors with windowing functions,” submitted to *IEEE Transactions on Electron Devices*, Feb. 2023.
 6. Li, J., B. Xiong, C. Sun, and Y. Luo, “Dual-drifting-layer uni-traveling carrier photodiode for wide bandwidth and high power performance,” *2015 Conference on Lasers and Electro-Optics (CLEO)*, San Jose, CA, USA, 2015.
 7. Williams, K. J., “Microwave nonlinearities in photodiodes,” PhD Dissertation, University of Maryland College Park, Maryland, USA, 1994.
 8. Razeghi, M., *Fundamentals of Solid State Engineering*, Springer, 2006.
 9. Hu, Y., “Modeling nonlinearity and noise in high-current photodetectors,” Ph.D. Dissertation, University of Maryland, Baltimore County, Maryland, USA, 2017.
 10. Scaburri, R., “The incomplete ionization of substitutional dopants in Silicon Carbide,” PhD Dissertation, University of Bologna, Bologna, Italy, 2011.
 11. Xiao, G., J. Lee, J. J. Lioua, and A. Ortiz-Conde, “Incomplete ionization in a semiconductor and its implications to device modeling,” *Microelectron. Reliab.*, Vol. 39, 1299–1303, 1999.
 12. Selberherr, S., *Analysis and Simulation of Semiconductor Devices*, Springer, 2012.
 13. Yang, K., J. C. Cowles, J. R. East, and G. I. Haddad, “Theoretical and experimental dc characterization of InGaAs-based abrupt emitter HBT’s,” *IEEE Trans. Electron Devices*, Vol. 42, 1047–1058, 1995.
 14. Wang, H. and G.-I. Ng, “Avalanche multiplication in InP/InGaAs double heterojunction bipolar transistors with composite collectors,” *IEEE Trans. Electron Devices*, Vol. 47, 1125–1133, 2000.
 15. Harris, F. J., “On the use of windows for harmonic analysis with the discrete Fourier transform,” *IEEE Proc.*, Vol. 66, 5–83, 1978.
 16. Nuttall, A. H., “Some windows with very good sidelobe behavior,” *IEEE Trans. Acoust. Speech Signal Process*, Vol. 29, No. 1, 1981.
 17. Nahory, R. E., M. A. Pollack, W. D. Johnston, Jr., and R. L. Barns, “Band gap versus composition and demonstration of Vegard’s law for $\text{In}_{1-x}\text{Ga}_x\text{As}_y\text{P}_{1-y}$ lattice matched to InP,” *Appl. Phys. Lett.*, Vol. 33, 659–661, 1978.